



Structural modification of LaCoO₃ perovskite for oxidation reactions: The synergistic effect of Ca²⁺ and Mg²⁺ co-substitution on phase formation and catalytic performance



Jingyi Zhang, Dongdong Tan, Qingjie Meng, Xiaole Weng*, Zhongbiao Wu

Department of Environmental Engineering, Zhejiang University, Zhejiang Provincial Engineering Research Centre of Industrial Boiler & Furnace Flue Gas Pollution Control, Hangzhou 310058, PR China

ARTICLE INFO

Article history:

Received 8 October 2014

Received in revised form 2 February 2015

Accepted 9 February 2015

Available online 11 February 2015

Keywords:

Perovskite

Catalytic oxidation

Mg

Ca

VOCs

ABSTRACT

Ca²⁺ and/or Mg²⁺ modified LaCoO₃ perovskites were synthesized via a continuous supercritical water (sc-H₂O) route, followed by a suite of heat-treatment processes. Experimental results revealed that the introductions of Ca²⁺ and Mg²⁺ had profoundly hindered the crystal growths of La(OH)₃ and Co(OH)₂ crystallites in sc-H₂O environment where the extra Mg(OH)₂ had provided a confined platform for their reaction, effectively facilitating the formation of phase pure LaCoO₃ perovskite. The synergistic effect as induced by dual-site substitution of Ca²⁺ and Mg²⁺ was proven very beneficial for suprafacial oxidation process, which had reduced the apparent activation energy (E_a) of LaCoO₃ to only 34 kJ/mol in toluene oxidation. This is comparable to some noble metal catalysts. However, the dual-site substitution had somehow deactivated the intrafacial reaction process as the co-substituted Ca²⁺ had inhibited the generation of surface lattice oxygen and decreased the reducibility of LaCoO₃ perovskite.

© 2015 Elsevier B.V. All rights reserved.

1. Introduction

Perovskite oxides (with the formula of ABO₃) have a superior structure with a ReO₃-type framework built up by incorporation of A cations into BO₆ octahedron, where the A site is usually occupied by alkaline-earth, alkali or other larger ions and the B site was consisted of various transition metal cations with relatively smaller radius [1]. Owing to the presence of BO₆ octahedron, perovskites are capable to sustain excessive changes in their A and/or B sites by partially substituting other metal ions. This could induce structural distortions and/or B site valence transformations, hence altering their physiochemical properties for various applications [2,3].

Recently, lanthanum-based perovskites have attracted tremendous interests, which have been extensively employed as catalysts in the applications such as soot combustion for automotive exhaust treatments [4,5], methane reforming for hydrogen productions [6], volatile organic compounds (VOCs) oxidation for air pollution controls [7,8]. The low cost, great diversity, high thermal stability and

mechanical strength make these perovskites very promising materials for catalysis applications. However, up to now, the catalytic performances of lanthanum-based perovskites are still not satisfied for industrial applications, which have been severely hindered by their low surface areas and high-temperature aged structures (i.e., the structures with limited amounts of defects). As such, significant efforts have been made in current science to develop advanced perovskites with better catalytic performances where the vast majority of works are focused on structurally modifying the A and/or B sites (via metal ion substitutions) to yield more defective structures. For examples, Magalhães et al. [9] had substituted Ce⁴⁺ into the A site of LaCoO₃, which favored the oxygen vacancies and O²⁻ storage and hence enhanced the selective CO oxidation reaction (SRLOX); Pereñíguez et al. [10] had studied the Sr²⁺ modified LaCoO_{3-δ}, indicating that the Sr substitution could promote the chemisorbed oxygen species over the LaCoO_{3-δ}, hence improving its catalytic performance in toluene oxidation; Barbero et al. [11] and Pecchi et al. [12] had substituted Ca²⁺ into the A site of LaFeO₃ lattice, which effectively raised their B site valences from Fe³⁺ to Fe⁴⁺ and hence promoted their catalytic performances; Merino et al. [13] had substituted the Ca²⁺ into LaCoO₃ lattice, which distinctly increased its surficial oxygen vacancy densities, hence yielding promoted catalytic activities for propane oxidation; Yan et al. [14] had conducted a series of B site substitutions over LaCoO₃ perovskite, which indicated that the substitutions of Mn²⁺, Fe²⁺, Ni²⁺, Cu²⁺ could lead

Abbreviations: CHFS, continuous hydrothermal flow synthesis; sc-H₂O, supercritical water; LC, LaCoO₃; LCC, La_{0.9}Ca_{0.1}CoO₃; LCM, LaCo_{1-x}Mg_xO₃/yMgO, where x + y = 1; LCCM, La_{0.9}Ca_{0.1}Co_{1-x}Mg_xO₃/yMgO, where x + y = 1.

* Corresponding author. Tel: +86 571 87953088; fax: +86 571 87953088.

E-mail address: xlweng@zju.edu.cn (X. Weng).

to an enhancement in CO oxidation whilst that of Cr^{2+} had, however, resulted in an opposite effect. Nevertheless, there are plenty of works can be referred from the literature in structural modifications over the perovskites [15], which have indeed resulted in a range of outcomes in terms of defective structures and catalytic activity improvements. However, the vast majority of works are focused on the investigations onto the effect of single-site (either A or B site) modification, where studies on dual-site modifications are still limited. As a matter of fact, the dual-site modification ought to be raised more attentions as its resulted synergistic effect could be more complicated than that of single-site modification and might not be always beneficial for all catalytic oxidation processes [16,17]. With this in mind, in this paper, we have conducted a series of single/dual-site modifications over a lanthanum-based perovskite where their effects on the generations of different active oxygen species and the kinetics of various oxidation processes were evaluated. We expect that the work conducted herein could provide some guidelines for structural modifications over the A and/or B sites of perovskites to yield more advanced properties.

LaCoO_3 as being previously reported easy to form surface anion vacancies [1] was selected as a base material for structural modification. A well-reported Ca^{2+} was chosen for A site modification [11–13] whilst a Mg^{2+} was selected for B site modification owing to its MgO was a well-known sintering barrier, the over-loading of which could not only hinder the agglomeration and growth of LaCoO_3 crystallites during the calcination process but also enhance their catalytic activities via the Mg^{2+} substitution [18,19]. The relationship between the varied sites modifications and the catalytic performances and reaction kinetics of LaCoO_3 perovskites was evaluated using a range of analytical techniques including XRD, HR-TEM, H_2 -TPR, O_2 -TPD, XPS, etc. Toluene and methane oxidation processes [20,21] that were corresponded to suprafacial and intrafacial reactions over the LaCoO_3 perovskite, respectively, were selected as the probes to measure the effects of different active oxygen species (as resulted by the structural modifications) on respective oxidation processes [22].

2. Experimental details

2.1. Continuous hydrothermal flow synthesis (CHFS)

The syntheses of $\text{La}(\text{OH})_3$, $\text{Co}(\text{OH})_2$ and $\text{Mg}(\text{OH})_2$ precursors for the fabrications of LaCoO_3 , $\text{LaCoO}_3/\text{MgO}$ (molar ratio at 1:1) and their Ca modified samples had been reported in our previous work [19]. The resulted as-prepared precursor was subsequently heat-treated in static air at designed temperatures to yield $\text{LaCoO}_3/\text{MgO}$ composite perovskite (denoted as LCM), LaCoO_3 (denoted as LC), $\text{La}_{0.9}\text{Ca}_{0.1}\text{CoO}_3$ (denoted as LCC) and $\text{La}_{0.9}\text{Ca}_{0.1}\text{CoO}_3/\text{MgO}$ (denoted as LCCM), respectively. Their corresponding precursors were denoted as A-LC, A-LCC, A-LCCM, A-LCM, respectively.

2.2. Characterizations

An Optima 7300 DV ICP supplied from PerkinElmer Corporation (USA) was used to measure the metal ion contents in the samples. XRD patterns were recorded by a Rigaku D/Max RA diffractometer with $\text{Cu-K}\alpha$ radiation ($\lambda = 0.15418 \text{ nm}$) at 40 kV and 150 mA and at an angle of 2θ from 10 to 80° . The morphologies of perovskites were investigated using a model Tecnai G² F20 S-TWIN (FEI Company, USA) high-resolution transmission electron microscope (HR-TEM, 400 kV accelerating voltage). BET surface areas (BET) were determined using N_2 physisorption at 77 K, with a Micromeritics ASSP 2020 equipment. Sample degassing pre-treatment was conducted at 150°C for 2 h under vacuum. Surface elemental analysis was carried out by XPS using a Thermo ESCALAB 250 instrument with

Al-K α radiation (photon energy 1486.6 eV) at 150 W. The signal of adventitious carbon (a binding energy of 284.6 eV) had been used to calibrate the binding energy scale for XPS measurements.

2.2.1. H_2 -TPR

The details of H_2 -TPR test were as follows: step 1 (pre-treatment step) in which samples (0.05 g) were heated to 400°C with a dwelling time of 1 h and then cooled down to room temperature. The process was operated with a purge of flowing O_2/He (3% O_2 in He) gas at the rate of 50 mL/min; step 2 (TPR step) in which samples were pre-treated at 100°C for 40 min and then heated up from 100 to 900°C under a purge of flowing H_2/N_2 (6% H_2 in N_2) at 35 mL/min. The variation in H_2 concentration was recorded by a thermal conduction detector (TCD).

2.2.2. O_2 -TPD

0.1 g sample was pre-treated at 500°C for 2 h with a purge of flowing O_2 gas at the rate of 30 mL/min; After the temperature was slowly cooled down to room temperature at a ramp of $2^\circ\text{C}/\text{min}$, followed by a He purge with a flow rate of 50 mL/min for 40 min, the sample was heat-treated from 40 to 1000°C and remained at 1000°C for 30 min. The signal of desorbed oxygen was monitored by a quadrupole mass spectrometer (Hiden Analytical Ltd., UK) and calibrated by a pulse of pure O_2 with 86.5 μL volume.

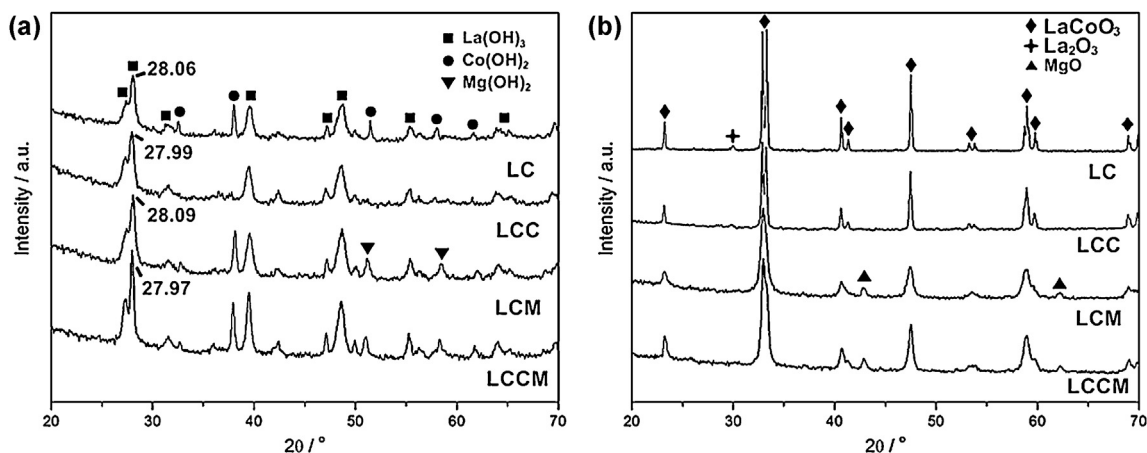
2.3. Catalytic oxidation test

2.3.1. Toluene oxidation test

The activities of samples were measured in a fixed bed reactor. The 6-mm i.d. quartz reactor tube was loaded with 0.50 g catalyst powder (40–60 mesh, mixed with quartz sand to yield the totally volume at 1 mL) and placed in an electrically heated furnace. The flow rate was set to maintain the gas hourly space velocity (GHSV) at 19,200 mL/(gh) for all the runs. The nitrogen streams were bubbled through a saturator filled with liquid toluene (flow rate = 1.6 mL/min) and water (flow rate = 40 mL/min) in a water bath at 10°C and 50°C , respectively, which were then mixed with 10% O_2/N_2 gas stream to keep the inlet concentration of gaseous toluene at ca. 500 ppm and water at ca. 3 vol%. Prior to the tests, all samples were pre-treated under a purge of the mixed gas at 120°C until the stabilization of the system. The reactants and products were monitored using GC analyzer (Agilent Technologies 7890A) equipped with a flame ionization detector (FID) and GS-Gaspro column. No other carbon-containing organic compounds were detected at T_{90} (i.e., 90% conversion of toluene). The statistical error for the test were estimated less than 1%. As for the kinetic parameter measurements, the experiments were performed without the introduction of water, where the reaction rate constant (k) was calculated by the reactant conversion rate and GHSV and the apparent activation energy (E_a) were evaluated by applying the Arrhenius plots. The external diffusion were excluded through a series of mass transfer tests (see Fig. S1) over the catalysts whereas the internal diffusion could be generally ignored if the particle sizes were less than 0.4 mm (i.e., 40–60 mesh) [11–13,23–25].

2.3.2. Methane oxidation test

The activities of samples were measured in a fixed bed reactor. The 8 mm i.d. steel tube was loaded with 0.50 g catalyst powder (40–60 mesh, mixed with quartz sand to yield the totally volume at 1 mL) and placed in an electrically heated furnace. The flow rate was set to maintain the gas hourly space velocity (GHSV) at 19,200 mL/(gh) for all the runs. The reactant feed rate (total at 160 mL/min) was controlled by mass flow controllers containing 1 vol% CH_4 , 10 vol% O_2 and 3 vol% water with balance N_2 . Prior to the tests, all samples were pretreated at 500°C for 1 h under a purge



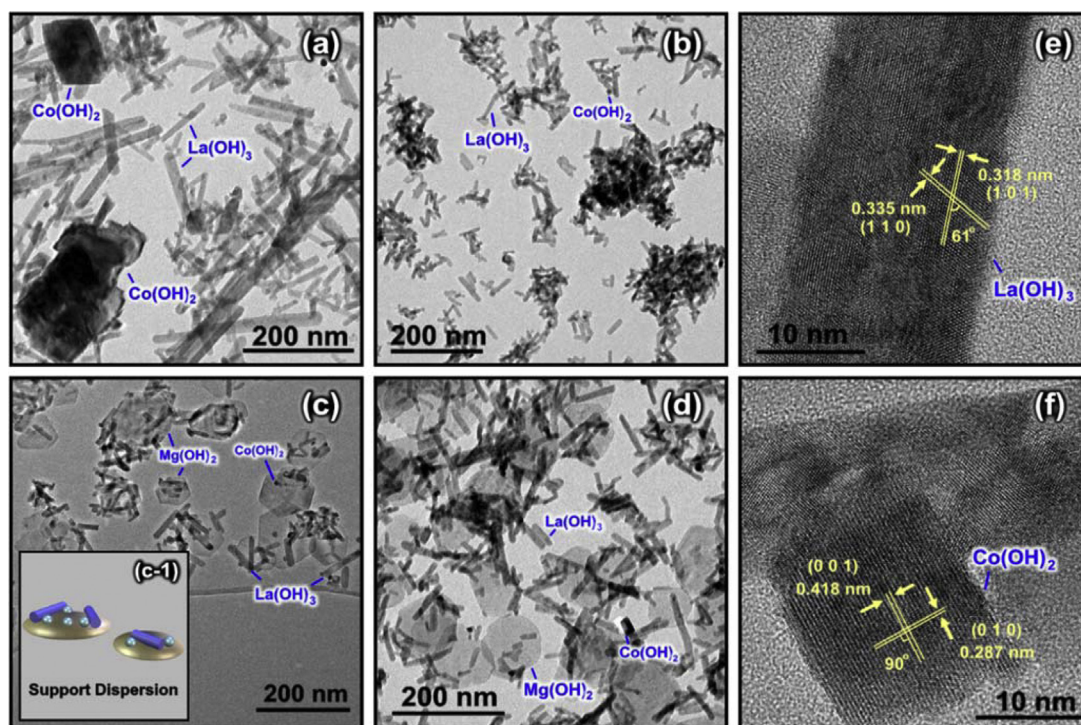


Fig. 2. HR-TEM images of (a) A-LC sample, (b) A-LCC sample, (c) A-LCM sample and (d) A-LCCM sample. The simulation model present in (c-1) represents the “support dispersion” feature of the A-LCM and A-LCCM samples whilst (e) and (f) show the d-spacing of $\text{La}(\text{OH})_3$ and $\text{Co}(\text{OH})_2$ crystallites, respectively.

broadening. It can be seen that the substitution of Ca^{2+} did not obviously change the crystal domain size of LaCoO_3 perovskite whilst the Mg^{2+} modification had caused a significant size decrease in LCM and LCCM samples. This is unsurprisingly given that the MgO would act as sintering barriers to inhibit the crystal growth of LaCoO_3 perovskite [18,19] during its calcination. One might argue that such varied crystal sizes could be due to their different calcination temperatures [29]. As such, we have heat-treated the LCM sample at 900°C for 2 h, which still showed a much lower crystal size (at ca. 85 nm, data not shown) than the LCC sample (at ca. 250 nm). This further confirmed the inhibition effect of MgO on the sintering of LaCoO_3 perovskite. The BET surface areas of each sample was consistent with their crystal domain sizes where the LCM and LCCM samples revealed much higher surface areas than the LC and LCC samples although the extra MgO phase might make some contributions.

Rietveld refinement analyses were performed to evaluate the structural configurations of LaCoO_3 perovskite in each sample. As shown in Table 1, the LaCoO_3 in LC sample was evaluated with a rhombohedral symmetry of the space group (R-3c). It was found that the substitution of Ca^{2+} did not cause an obvious lattice parameter (a) elongation in LCC sample, which could be due to the similar ionic radius of Ca^{2+} (at ca. 0.100 nm) and La^{3+} (at ca. 0.103 nm) as presented in LaCoO_3 perovskite. However, Ca^{2+} substitution had slightly decreased the angle (α) of rhombohedral unit cell, implying a structural distortion was occurred in the LCC sample, which

was consistent with the previous reports [10,13]. For Mg^{2+} substitutions, the LCM sample revealed a relatively larger lattice parameter (a) than the LC sample, yielding a slightly structural expansion for the sample (where unit cell volume for LC sample at 112.0 \AA^3 and for LCM sample at 112.4 \AA^3). The reason could be ascribed to the partial insertion of Mg^{2+} ions (ionic radius = 0.072 nm) into the relatively smaller B site sub-lattice (Co^{3+} ionic radius = 0.063 nm) of the LaCoO_3 perovskite, leading to an elongation in lattice parameter (a) and an expansion in unit cell in LCM sample. The substitution of Mg^{2+} had also caused a decrease in unit cell angle (α), the extent of which was relatively larger than that induced by Ca^{2+} substitution, implying a more severe distortion as caused by Mg^{2+} substitution. Further substitution of Ca^{2+} into the LCM sample had yielded an even lower unit cell angle (α), indicating a synergistic effect being raised by the dual-site modification, which caused a more severely structural distortion in LCCM sample.

3.2. X-ray Photoelectron spectroscopy

Zhang et al. [1] had indicated that the distortion of perovskites could lead to oxygen non-stoichiometries in their structures, which would generate trace amounts of oxygen vacancies as well as weakly chemisorbed oxygen species over the surfaces. To verify this, XPS analyses were then conducted on each sample. Generally, in Co2p XPS spectra, the bands at ca. 779.7 eV ($\text{Co } 2p_{1/2}$) and ca. 795.0 eV ($\text{Co } 2p_{3/2}$) were indicative of Co^{3+} chemical state whilst

Table 1
The constitutional molar ratios, specific BET surface areas and lattice parameters for each sample.

Samples	Chemical compositions	BET/ $\text{m}^2 \text{ g}^{-1}$	d/nm	Lattice parameters		
				a/ \AA	$\alpha/^\circ$	R/%
LC	LaCoO_3	5.9	34.3	5.378	60.78	3.95
LCC	$\text{La}_{0.94}\text{Ca}_{0.06}\text{Co}_{1.13}\text{O}_3$	3.9	30.6	5.379	60.75	4.71
LCM	$\text{LaCo}_{1.13}\text{Mg}_x\text{O}_{3+y}/\text{MgO } x+y=1.17$	27.4	14.3	5.388	60.70	2.75
LCCM	$\text{La}_{0.94}\text{Ca}_{0.06}\text{Co}_{1.06}\text{Mg}_x\text{O}_{3/y}/\text{MgO } x+y=0.94$	24.3	14.8	5.391	60.65	3.86

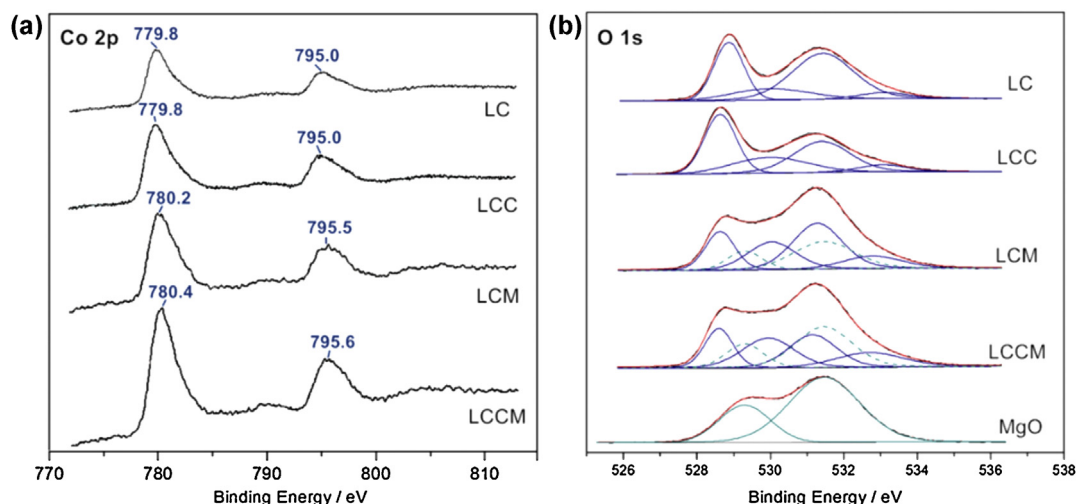


Fig. 3. XPS spectra of (a) Co2p bands and (b) O 1s bands for each sample.

the bands at ca. 781.4 eV ($\text{Co } 2p_{1/2}$) and ca. 796.5 eV ($\text{Co } 2p_{3/2}$) were corresponded to Co^{4+} [30]. However, due to their relatively close characteristic bands, distinguishing Co^{3+} and Co^{4+} barely based on peak fittings is difficult. Nevertheless, their transformation could be still evaluated in terms of the corresponding BE bands shifting where the higher band shifting was indicative of a transformation from Co^{3+} to Co^{4+} in the sample [18]. It was found that the LCC sample (see Fig. 3a) did not reveal an obvious BE shifting compared with the LC sample, which implied that the Ca^{2+} substitution did not induce a Co^{3+} to Co^{4+} transformation in the sample, according well with the reports by Merino et al. [13,31]. By comparison, the LCM sample showed a relatively higher BE value shifting compared with the LC sample, which indicated that the Mg^{2+} substitution had resulted in a transformation from Co^{3+} to Co^{4+} in the sample. This is unsurprisingly given that the lower-valence ion substitution of Mg^{2+} could raise the B site valence of LaCoO_3 perovskite to compensate its structure charge neutrality [31]. Surprisingly, the substitution of Ca^{2+} into the LCM sample had further shifted its Co2p bands to higher BE value range. This indicated that unlike the LCC sample, the Ca^{2+} substitution together with the Mg^{2+} could yield a synergistic effect on B site valence rising, where the co-substituted Ca^{2+} had further stabilized the Co^{4+} chemical state in the LCCM sample.

Fig. 3b revealed the fitted O1s peaks of lattice oxygen species (O^{2-} , denoted as O_{lat}) at 528.6–528.8 eV [31–33], chemisorbed oxygen species (O^- and O_2^- , denoted as O_{ad}) at 530.0–530.4 eV [31,34], hydroxyl groups or carbonate species at 531.2–531.4 eV [31,33] and adsorbed molecular water at 532.7–533.1 eV [31,35,36] in each sample. It should be noted that since the LCM and LCCM samples were both contain a proportional of extra MgO phase, their peak fittings should take the O1s peaks of MgO (peaks at 529.3 and 531.4 eV were assigned to lattice oxygen and hydroxyl groups, respectively [37]) into account. As shown in Table 2, an enrichment of La element was observed in all samples. This was also the case for Ca element in the LCC and LCCM samples. It was found that the substitution of Ca^{2+} had only slightly increased the $\text{O}_{\text{ad}}/\text{O}_{\text{lat}}$ ratio in LCC sample whilst the substitution of Mg^{2+} had remarkably increased the $\text{O}_{\text{ad}}/\text{O}_{\text{lat}}$ ratio in LCM sample. One may argue that this difference could be ascribed to the varied doping levels of Ca^{2+} and Mg^{2+} in the LCC and LCM sample, respectively. Indeed, the amount of Ca^{2+} substitution in LCC sample could be easily measured by using ICP technique (that was at 0.06, see Table 1) whilst that of Mg^{2+} was difficult to be quantitatively measured. However, Ramadass et al. had reported that the solid solubility of Mg^{2+} in LaCoO_3 perovskite was generally less than 10 mol% [38], which was relatively close to

the stoichiometry of Ca^{2+} in LCC sample. As such, the difference in $\text{O}_{\text{ad}}/\text{O}_{\text{lat}}$ ratios of the LCC and LCM samples should be correlated to their varied substitution sites, where it had been reported that the B site substitution was always playing a major role in the promotion of chemisorbed oxygen species over the perovskite surface [3]. Further substitution of Ca^{2+} into the LCM sample had continuously raised the $\text{O}_{\text{ad}}/\text{O}_{\text{lat}}$ ratio in LCCM sample, which revealed ca. threefold higher value than that of the LC sample. This result is very promising as it implied a significant synergistic effect of the dual-site substitution on the promotion of chemisorbed oxygen species over the perovskite surface. In addition, the sequence of $\text{O}_{\text{ad}}/\text{O}_{\text{lat}}$ values (i.e., $\text{LCCM} > \text{LCM} > \text{LCC} > \text{LC}$) were in line well with their unit cell angles (α , see Table 1), implying that the change in unit cell angle was truly correlated with the formation of oxygen vacancies (due to structural distortion) as well as chemisorbed oxygen species over the perovskite surface [11].

3.3. O_2 -TPD Measurements

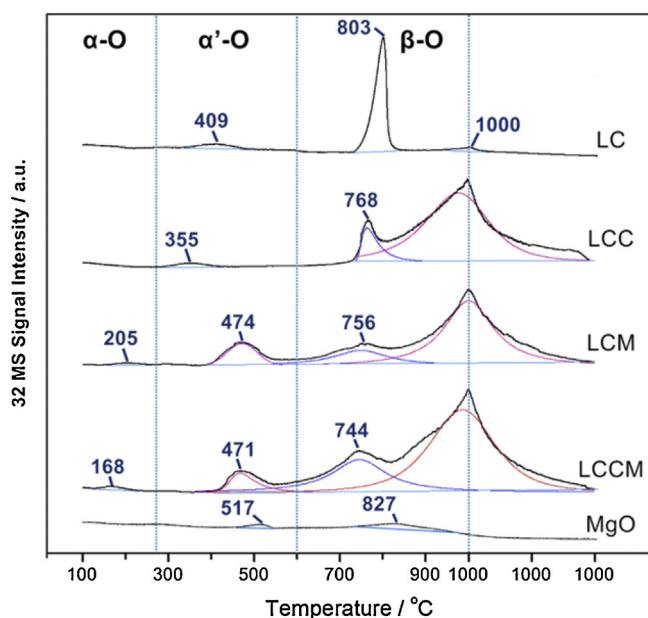
To get insight into the various oxygen active species as resulted by the A and/or B site modifications over the LaCoO_3 perovskite, O_2 -TPD were conducted within the temperature range of 100–1000 °C for each sample. A prolonged aging at 1000 °C was conducted to ensure the complete desorption of lattice oxygen species from the perovskite. Generally, the O_2 -TPD plots for LaCoO_3 perovskite were consisted of three oxygen desorption regions as indicated in Fig. 4, where the lower temperature region (denoted as α -O) is corresponded to weakly chemisorbed oxygen upon oxygen vacancies [39,40], the intermediate region (denoted as α' -O) is ascribed to surface lattice oxygen (denoted as α' -O) that is generated from the dislocations and grain frontiers [10] and the higher temperature region (denoted as β -O) is assigned to lattice oxygen [10,41], which could cause the reduction of B site cations [42–44]. In this paper, the highest temperature region (i.e., the onset temperature ≥ 900 °C) was not evaluated as it beyond the scope of our investigation temperature range.

From Fig. 4, it can be seen that the LC and LCC samples did not show obvious α -O desorption peaks in the temperature range of 100–300 °C, where the LCM and LCCM samples revealed the distinct α -O desorption peaks centered at 205 °C and 168 °C, respectively. This result was consistent with their XPS analyses, which gave that the LCM and LCCM samples possessed much higher $\text{O}_{\text{ad}}/\text{O}_{\text{lat}}$ ratios than the LC and LCC samples (see Table 2). After peak integration measurements, the LCCM sample revealed a nearly twofold higher

Table 2

The surface elemental analyses of each sample.

Samples	La/Co	Ca/La	(La + Ca)/Co	O				
				O _{H₂O} BE/eV	O _{OH⁻} BE/eV	O _{ad} BE/eV	O _{lat} BE/eV	O _{ad} /O _{lat}
LC	2.05	–	–	533.1	531.4	530.0	528.9	0.51
LCC	1.36	0.26	1.70	533.1	531.4	530.0	528.6	0.61
LCM	1.80	–	–	532.8	531.2	530.0	528.6	1.16
LCCM	1.44	0.88	2.72	532.7	531.2	530.0	528.6	1.41

**Fig. 4.** O₂-TPD profiles for each sample.

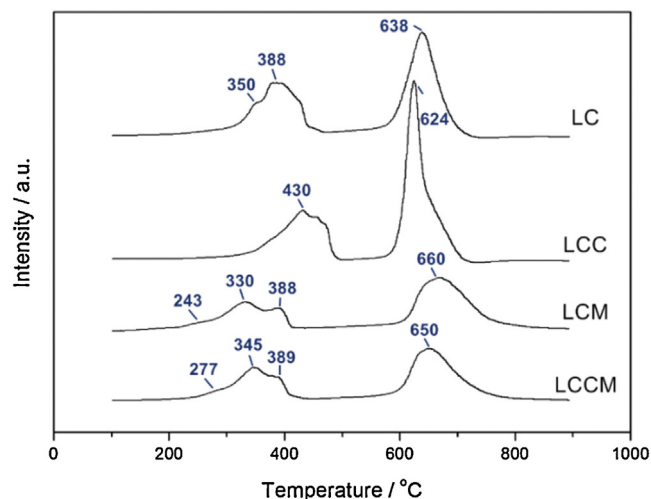
α-O desorption value than the LCM sample (see Table 3), which was also consistent with their XPS results.

For the measurements of α'-O desorption, the LCC sample revealed a much lower desorption peak (at ca. 355 °C) than the LC sample (at ca. 409 °C), indicating that the substitution of Ca²⁺ had increased the mobility of surface lattice oxygen species (i.e., α'-O) over the LaCoO₃ perovskite. The reason could be ascribed to the increased oxygen vacancies as induced by Ca²⁺ substitution (see Table 2) that had facilitated the movement of α'-O toward the perovskite surface [45]. However, peak integration measurements (see Table 3) had revealed that the LCC sample possessed a much lower α'-O value than the LC sample, indicating that the substitution of Ca²⁺ had resulted in a negative effect on the generation of surface lattice oxygen species over the LaCoO₃ perovskite. By comparison, the LCM sample revealed a remarkable α'-O value than the LC sample, where further substitution of Ca²⁺ had again decreased the α'-O value in LCCM sample. For β-O desorption, both the Ca²⁺ and Mg²⁺ substitutions had effectively decreased the amounts of β-O. However, in the presence of Mg²⁺, further substitution of Ca²⁺ had surprisingly increased the amount of β-O in LCCM sample, revealing a promising synergistic effect of the Ca²⁺ and Mg²⁺ dual substitution on the generation of lattice oxygen species over the LaCoO₃ perovskite.

Table 3

The amounts of various active oxygen species in each sample.

Samples	α-O/μmol/g	α'-O/μmol/g	β-O/μmol/g
LC	–	6.2	70.1
LCC	–	2.7	17.3
LCM	0.9	19.9	37.4
LCCM	1.6	13.6	82.1

**Fig. 5.** H₂-TPR profiles for each sample.

3.4. H₂-TPR Measurements

Fig. 5 illustrates the H₂-TPR plots for each sample. As reported in literature [24], the hydrogen consumption over LaCoO₃ perovskite generally involved two regions, i.e., at 200–500 °C corresponding to the reduction of Co³⁺ to Co²⁺ and at 600–800 °C for the reduction of Co²⁺ to metallic cobalt (Co⁰). It can be seen that the LC sample revealed two distinct hydrogen consumption peaks centered at 350 and 388 °C, where the former was proposed due to the reduction of trace amounts of Co₃O₄ (see its XRD result) as a bulk Co₃O₄ (that was also synthesized via the CHFS route) had showed a close hydrogen consumption peak at 352 °C in its H₂-TPR plot (see Supplementary Fig. S3). After Ca²⁺ substitution, the LCC sample revealed an obviously higher temperature shift for its hydrogen consumption peaks, indicating a lower reducibility for the sample, which was consistent with the previous reports [11,46,47].

The substitution of Mg²⁺ had led to a distinct peak shifting to lower temperature range in LCM sample, where further substitution of Ca²⁺ had again caused a decreased reducibility in LCCM sample. One might notice that both the LCM and LCCM samples had distinctly lower peak intensities than the LC and LCC samples. This could be due to their extra MgO phase (that did not show obvious hydrogen reduction peaks within the investigated temperature range, see Supplementary Fig. S4) had resulted in the presence of relatively smaller amounts of LaCoO₃ in the samples. The consumption peaks centered at 243 °C, 330 °C and 388 °C for LCM sample and at 277 °C, 345 °C and 389 °C for LCCM sample were considered corresponding to the reductions of absorbed oxygen species (i.e., α-O and/or α'-O), Co⁴⁺ to Co³⁺ and Co³⁺ to Co²⁺, respectively [46], where the increased peak intensity for the reduction of Co⁴⁺ to Co³⁺ in LCCM sample was in good agreement with its XPS result, which indicated that the LCCM sample had more Co⁴⁺ chemical state than the LCM sample (see Fig. 3).

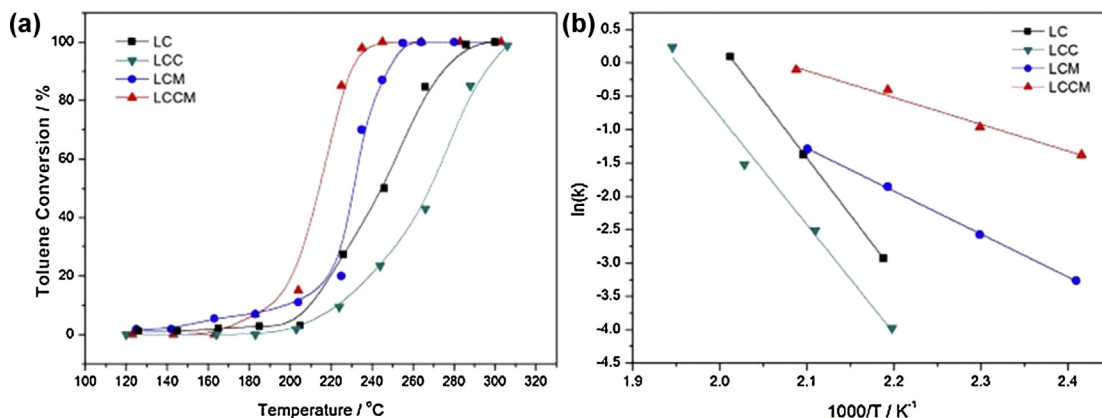


Fig. 6. (a) Toluene conversion rate with 3 vol% water (where gas hourly space velocity (GHSV) at 19,200 mL/(g h), toluene at ca. 500 ppm, N₂:143 mL/min, O₂:16 mL/min) and (b) Arrhenius plots for the reaction over each sample (the data was obtained without the presence of water).

3.5. Catalytic oxidation measurements

As reported [22], the catalytic oxidations over the perovskite generally follow two reaction mechanisms, defined as suprafacial mechanism (reaction temperature <400 °C), where the weakly chemisorbed oxygen (i.e., α -O) plays a crucial role in the oxidation process, and intrafacial mechanism (reaction temperature ≥ 400 °C) that was closely related to the amounts and mobility of surface lattice oxygen species (i.e., α' -O). As such, to evaluate the functionalities of Ca²⁺ and/or Mg²⁺ structural modifications over the LaCoO₃ perovskite on these two oxidation processes, two typical reactants, toluene and methane, were selected as the probes to simulate the suprafacial and intrafacial reactions, respectively.

In toluene oxidation measurements, the samples were all subjected to a feed stream containing ca. 500 ppm toluene and ca. 3 vol% water with a gas hourly space velocity (GHSV) at 19,200 mL/(g h). As shown in Fig. 6a, the LCCM sample revealed the highest catalytic activity with a light-off temperature (T_{50} , 50% conversion of toluene) at ca. 214 °C and a total oxidation temperature (T_{90} , i.e., 90% conversion of toluene) at ca. 228 °C. This result was consistent with the XPS (see Table 2) and O₂-TPD analyses (see Table 3), which indicated that the LCCM sample had the highest amounts of chemisorbed oxygen species (i.e., α -O). The LCM and LC samples showed an inferior toluene oxidation performance with the T_{90} at ca. 248 °C and 275 °C, respectively, where the trace amounts of Co₃O₄ in LC sample might provide a promotional role in enhancing its catalytic performance [27], leading to its activity higher than LCC sample (although the LC sample with lower O_{ad}/O_{lat} value, see Table 2). The LCC sample yielded the worst catalytic performance with the T_{50} at ca. 265 °C and T_{90} at ca. 295 °C. Compared to the performances in the absence of water (see Fig. S5a), the vast majority of catalysts did not show obvious suppression except for the LC sample, which revealed a distinct decrease in its T_{90} from ca. 255 °C to ca. 295 °C. The sequences of T_{50} and T_{90} in these samples had further confirmed that the chemisorbed oxygen species played a crucial role in the low-temperature oxidation process (i.e., suprafacial reaction mechanism) over the perovskites.

The kinetic parameters of each sample were calculated by considering that the toluene oxidation obeyed a first-order reaction mechanism [48,49]. The corresponding reaction rate equation was described as follow,

$$r = -kc = -A \exp\left(-\frac{E_a}{RT}\right) c \quad (1)$$

where r is the reaction rate (mol/(s mL)); k is the reaction rate constant (s⁻¹); A is the pre-exponential factor (s⁻¹) and E_a is the apparent activation energy (kJ/mol). The k value was calculated from the toluene conversion rate and the GHSV value. The A and E_a

Table 4

The kinetic parameters of each sample in toluene oxidation process.

Sample	$k \times 10^{-2} \text{ s}^{-1}$				E_a /kJ/mol	R^2
	140 °C	160 °C	180 °C	200 °C		
LC	—	—	5.3	25.3	143	0.986
LCC	—	—	1.9	8.1	135	0.984
LCM	3.81	7.62	15.6	27.4	53	0.988
LCCM	25.1	38.1	66.7	89.8	34	0.993

values were calculated by sloping and intercepting the Arrhenius plots at the reactant conversion rate less than 20%.

As shown in Fig. 6b, the Arrhenius plots for each sample were all linear dependence. The kinetic parameter calculations (see Table 4) had indicated that the LCCM sample possessed the highest k value and the lowest E_a value. These values were relatively close to those of macroporous Au/La_{0.6}Sr_{0.4}MnO₃ ($E_a = 44$ –48 kJ/mol) [23] and Au/LaCoO₃ ($E_a = 31$ –37 kJ/mol) [50] but significantly lower than that of Pt/Al₂O₃ ($E_a = 86$ kJ/mol) [51]. This result is very promising as it implies that the dual-site modification over the LaCoO₃ perovskite has yielded a very effective synergistic effect, which induced a comparable E_a value to some noble metal catalysts in the application of suprafacial oxidation process.

In methane oxidation measurements, the samples were all subjected to a feed stream containing 1 vol% methane and 3 vol% vapor with a gas hourly space velocity (GHSV) at 19,200 mL/(g h). Unlike the toluene oxidation, the LCCM sample herein did not revealed the highest catalytic activity but the LCM sample did, which showed the T_{50} at ca. 507 °C and the T_{90} at ca. 553 °C (see Fig. 7a). This result was in good accordance with the O₂-TPD (see Fig. 4) and H₂-TPR results (see Fig. 5). More importantly, the result illustrated that the dual-site substitution were not always beneficial for all catalytic oxidation processes. The sequence of catalytic performances for each sample was accorded well with their α -O values (see Table 3), which confirmed the significant role of the surficial oxygen species (i.e., α -O) in intrafacial oxidation processes. In addition, it was likely that the interior lattice oxygen (i.e., β -O) was not strongly correlated to the catalytic performance in intrafacial reactions as the LC sample that possessed the highest β -O value did not yield a promotional catalytic performance on its methane oxidation. This was also the case for the LCCM sample. Similar to toluene oxidation process, the presence of water also did not show obvious impact on the performances over these samples, except for the LCC sample, whose T_{50} was dropped from 550 °C to 590 °C (see Fig. S5b).

The dynamic parameter calculations for methane oxidation processes were also based on a first-order reaction mechanism [24,52]. As shown in Fig. 7b, a linear relationship of the Arrhenius plots was observed in all the samples. The calculation had revealed that the

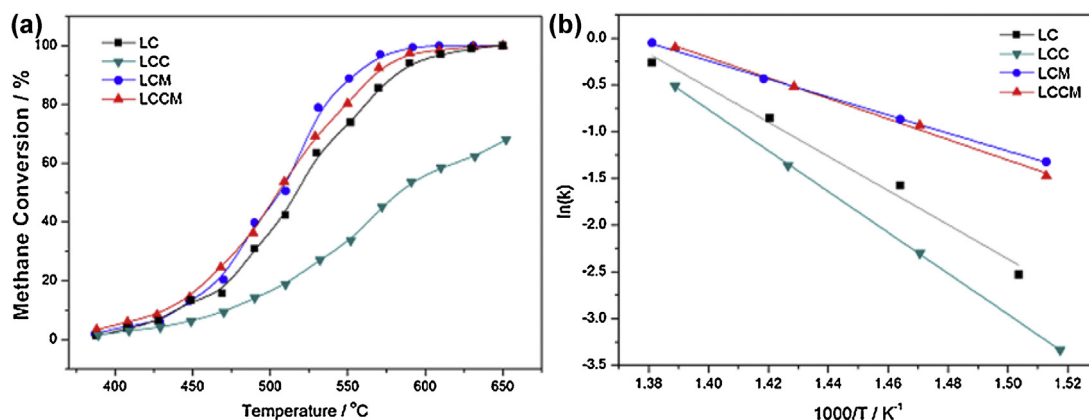


Fig. 7. (a) Methane conversion rate with 3 vol% (where gas hourly space velocity (GHSV) at 19,200 mL/(gh), methane at 1%, N₂:143 mL/min, O₂:16 mL/min) and (b) Arrhenius plots for the reaction over each sample (the data was obtained without the presence of water).

Table 5

The kinetic parameters of each sample in methane oxidation process.

Samples	$k \times 10^{-2} \text{ s}^{-1}$				Ea/kJ/mol	R ²
	390 °C	410 °C	430 °C	450 °C		
LC	7.9	20.6	42.5	76.8	152	0.980
LCC	3.6	10.0	25.6	59.9	181	0.998
LCM	26.7	41.9	64.7	95.2	80	0.999
LCCM	22.5	39.3	59.4	90.6	91	0.994

LCM sample possessed the highest k and the lowest Ea values as expected (see Table 5) and the sequences of k and Ea values in each sample were in accordance well with their catalytic performances as well as their α' -O values. The Ea values for the LCM sample (80 kJ/mol) was relatively close to those of BaZr_{1-x}M_xO₃ ($M = \text{Rh, Pd, Pt, Mn, Ni, Co}$) (Ea = 72–106 kJ/mol) [53] but significantly lower than those of La_{0.6}Sr_{0.4}Co_{0.2}Fe_{0.8}O_{3- δ} (Ea = 128 kJ/mol) [54] and CuO(or MnO_x)/Al₂O₃ (Ea = 120–144 kJ/mol) [55].

In summary, the synergistic effect as induced by Ca²⁺ and Mg²⁺ dual-site substitution over the LaCoO₃ perovskite (i.e., LCCM sample) was very beneficial for suprafacial reaction processes, owing to its distinct increase in the amounts of chemisorbed oxygen species over the perovskite surface. However, the dual-site substitution had induced a slight deactivation on the intrafacial reaction process as the co-substituted Ca²⁺ had inhibited the generation of α' -O and decreased the reducibility of LaCoO₃. We expect that the work conducted herein could provide some promising guidelines for the design and syntheses of a host of advanced perovskites with high catalytic performances to enforce their industrial applications.

4. Conclusions

The main conclusions of this paper were drawn as follows:

- (1) The introductions of Ca²⁺ and Mg²⁺ had profoundly hindered the crystal growths of La and Co metal oxides in sc-H₂O.
- (2) The “support dispersion” feature was very beneficial for solid state reaction processes where the presence of extra Mg(OH)₂ had not only provided a confined platform for La(OH)₃ and Co(OH)₂ reaction, but also acted as sintering barrier to inhibit the crystal growths of LaCoO₃ crystallites during the calcination process.
- (3) For single-site substitutions over the LaCoO₃ lattice, the A site substitution by Ca²⁺ had generated trace amounts of oxygen vacancies but decreased the reducibility of the perovskite. The B site substitution of Mg²⁺ had induced a valence rising from Co³⁺ to Co⁴⁺ and promoted both the α -O and α'' -O of the perovskite.

- (4) For dual-site substitutions over the LaCoO₃ lattice, the Ca²⁺ substitution had further promoted the transformation of Co³⁺ to Co⁴⁺ over the perovskite, which was different from its single-site substitution effect. The synergistic effect that was induced by the dual-site substitution was very beneficial for suprafacial oxidation process but showed a relatively negative effect on intrafacial oxidation process.
- (5) The developed LCCM (with high amounts of chemisorbed oxygen) and LCM samples (with high amounts of surface lattice oxygen) have shown relatively low Ea values in toluene and methane oxidations, respectively, which were both comparable to those of some noble metal catalysts.

Acknowledgements

This work was financially supported by the National Natural Science Foundation of China (Grant No. 51208458) and the Program for Zhejiang Leading Team of S&T Innovation (Grant No. 2013TD07).

Appendix A. Supplementary data

Supplementary data associated with this article can be found, in the online version, at <http://dx.doi.org/10.1016/j.apcatb.2015.02.006>.

References

- [1] R. Zhang, N. Luo, B. Chen, S. Kaliaguine, Energy Fuels 24 (2010) 3719–3726.
- [2] N.A. Merino, B.P. Barbero, P. Ruiz, L.E. Cadús, J. Catal. 240 (2006) 245–257.
- [3] H.M. Zhang, Y. Shimizu, Y. Teraoka, N. Miura, N. Yamazoe, J. Catal. 121 (1990) 432–440.
- [4] C.H. Kim, G. Qi, K. Dahlberg, W. Li, Science 327 (2010) 1624–1627.
- [5] N. Russo, D. Fino, G. Saracco, V. Specchia, J. Catal. 229 (2005) 459–469.
- [6] D.A. Slade, A.M. Duncan, K.J. Nordheden, S.M. Staggs-Williams, Green Chem. 9 (2007) 577–581.
- [7] M. Alifanti, M. Florea, V.I. Pârvulescu, Appl. Catal. B 70 (2007) 400–405.
- [8] M. Zawadzki, J. Trawczyński, Catal. Today 176 (2011) 449–452.
- [9] R.N.S.H. Magalhães, F.S. Toniolo, V.T. da Silva, M. Schmal, Appl. Catal. A 388 (2010) 216–224.
- [10] R. Pereñíguez, J.L. Hueso, F. Gaillard, J.P. Holgado, A. Caballero, Catal. Lett. 142 (2012) 408–416.
- [11] B.P. Barbero, J.A. Gamboa, L.E. Cadús, Appl. Catal. B 65 (2006) 21–30.
- [12] G. Pecchi, M.G. Jiliberto, E.J. Delgado, L.E. Cadús, J.L.G. Fierro, J. Chem. Technol. Biotechnol. 86 (2011) 1067–1073.
- [13] N.A. Merino, B.P. Barbero, P. Grange, L.E. Cadús, J. Catal. 231 (2005) 232–244.
- [14] X. Yan, Q. Huang, B. Li, X. Xu, Y. Chen, S. Zhu, S. Shen, J. Ind. Eng. Chem. 19 (2013) 561–565.
- [15] J. Zhu, H. Li, L. Zhong, P. Xiao, X. Xu, X. Yang, Z. Zhao, J. Li, ACS Catal. 4 (2014) 2917–2940.
- [16] G. Zhang, Z. Zhao, J. Liu, J. Xu, Y. Jing, A. Duan, G. Jiang, J. Rare Earth 27 (2009) 955–960.
- [17] Z. Li, M. Meng, Y. Zha, F. Dai, T. Hu, Y. Xie, J. Zhang, Appl. Catal. B 121–122 (2012) 65–74.

- [18] S. Sun, L. Yang, G. Pang, S. Feng, *Appl. Catal. A* 401 (2011) 199–203.
- [19] J. Zhang, X. Weng, Z. Wu, Y. Liu, H. Wang, *Appl. Catal. B* 126 (2012) 231–238.
- [20] R. Pereñíguez, J.L. Hueso, J.P. Holgado, F. Gaillard, A. Caballero, *Catal. Lett.* 131 (2009) 164–169.
- [21] Y. Liu, H. Dai, Y. Du, J. Deng, L. Zhang, Z. Zhao, C.T. Au, *J. Catal.* 287 (2012) 149–160.
- [22] R.J.H. Voorhoeve, J.P. Remeika, L.E. Trimble, *Ann. N.Y. Acad. Sci.* 272 (1976) 3–21.
- [23] Y. Liu, H. Dai, J. Deng, X. Li, Y. Wang, H. Arandiyani, S. Xie, H. Yang, G. Guo, *J. Catal.* 305 (2013) 146–153.
- [24] H. Arandiyani, H. Dai, J. Deng, Y. Liu, B. Bai, Y. Wang, X. Li, S. Xie, J. Li, *J. Catal.* 307 (2013) 327–339.
- [25] D. Mukai, Y. Murai, T. Higo, S. Tochiya, T. Hashimoto, Y. Sugiura, Y. Sekine, *Appl. Catal. A* 466 (2013) 190–197.
- [26] G. Pecchi, P. Reyes, R. Zamora, L.E. Cadús, J.L.G. Fierro, *J. Solid State Chem.* 181 (2008) 905–912.
- [27] J. Deng, H. Dai, H. Jiang, L. Zhang, G. Wang, H. He, C.T. Au, *Environ. Sci. Technol.* 44 (2010) 2618–2623.
- [28] L. Predoana, B. Malic, M. Kosec, M. Carata, M. Caldararu, M. Zaharescu, *J. Eur. Ceram. Soc.* 27 (2007) 4407–4411.
- [29] Y. Zhu, R. Tan, T. Yi, S. Ji, X. Ye, L. Cao, *J. Mater. Sci.* 35 (2000) 5415–5420.
- [30] J.C. Dupin, D. Gonbeau, H. Benqilou-Moudden, P. Vinatier, A. Levasseur, *Thin Solid Films* 384 (2001) 23–32.
- [31] N.A. Merino, B.P. Barbero, P. Eloy, L.E. Cadús, *Appl. Surf. Sci.* 253 (2006) 1489–1493.
- [32] P. Xiao, J. Zhu, H. Li, W. Jiang, T. Wang, Y. Zhu, Y. Zhao, J. Li, *ChemCatChem* 6 (2014) 1774–1781.
- [33] Y. Wang, J. Ren, Y. Wang, F. Zhang, X. Liu, Y. Guo, G. Lu, *J. Phys. Chem. C* 112 (2008) 15293–15298.
- [34] L. Richter, S.D. Bader, M.B. Brodsky, *Phys. Rev. B* 22 (1980) 3059–3064.
- [35] X. Weng, J. Zhang, Z. Wu, Y. Liu, *Catal. Today* 175 (2011) 386–392.
- [36] H. Liang, Y. Hong, C. Zhu, S. Li, Y. Chen, Z. Liu, D. Ye, *Catal. Today* 201 (2013) 98–102.
- [37] Y.V. Larichev, B.L. Moroz, V.I. Zaikovskii, S.M. Yunusov, E.S. Kalyuzhnaya, V.B. Shur, V.I. Bukhtiyarov, *J. Phys. Chem. C* 111 (2007) 9427–9436.
- [38] N. Ramadass, J. Gopalakrishnan, M.V.C. Sastri, *J. Less Common Met.* 65 (1979) 129–138.
- [39] B. Białobok, J. Trawczyński, W. Miśta, M. Zawadzki, *Appl. Catal. B* 72 (2007) 395–403.
- [40] M. James, T. Tedesco, D.J. Cassidy, R.L. Withers, *Mater. Res. Bull.* 40 (2005) 990–1000.
- [41] S. Royer, H. Alamdari, D. Duprez, S. Kaliaguine, *Appl. Catal. B* 58 (2005) 273–288.
- [42] R. Zhang, H. Alamdari, S. Kaliaguine, *J. Catal.* 242 (2006) 241–253.
- [43] R. Zhang, A. Villanueva, H. Alamdari, S. Kaliaguine, *Appl. Catal. B* 64 (2006) 220–233.
- [44] A. Machocki, T. Ioannides, B. Stasinska, W. Gac, G. Avgouropoulos, D. Delimaris, W. Grzegorzczak, S. Pasieczna, *J. Catal.* 227 (2004) 282–296.
- [45] S. Royer, D. Duprez, S. Kaliaguine, *J. Catal.* 234 (2005) 364–375.
- [46] J. Xu, J. Liu, Z. Zhao, C. Xu, J. Zheng, A. Duan, G. Jiang, *J. Catal.* 282 (2011) 1–12.
- [47] S. Ponce, M.A. Peña, J.L.G. Fierro, *Appl. Catal. B* 24 (2000) 193–205.
- [48] D.D. Agarwal, H.S. Goswami, *React. Kinet. Catal. Lett.* 53 (1994) 441–449.
- [49] M. Alifanti, M. Florea, S. Somacescu, V.I. Parvulescu, *Appl. Catal. B* 60 (2005) 33–39.
- [50] X. Li, H. Dai, J. Deng, Y. Liu, S. Xie, Z. Zhao, Y. Wang, G. Guo, H. Arandiyani, *Chem. Eng. J.* 228 (2013) 965–975.
- [51] J. Łojewska, A. Kołodziej, P. Dynarowicz-Łątka, A. Weselucha-Birczyńska, *Catal. Today* 101 (2005) 81–91.
- [52] G. Landi, P.S. Barbato, A. Di Benedetto, R. Pirone, G. Russo, *Appl. Catal. B* 134–135 (2013) 110–122.
- [53] K. Gallucci, P. Villa, G. Groppi, N. Usberti, G. Marra, *Catal. Today* 197 (2012) 236–242.
- [54] N. Lakshminarayanan, H. Choi, J.N. Kuhn, U.S. Ozkan, *Appl. Catal. B* 103 (2011) 318–325.
- [55] S.M. Sager, D.I. Kondarides, X.E. Verykios, *Appl. Catal. B* 103 (2011) 275–286.